Reversible switching between superhydrophobic states on a hierarchically structured surface

Tuukka Verho[a], Juuso T. Korhonen[a], Lauri Sainiemi[b,c], Ville Jokinen[c], Chris Bower[d], Kristian Franze[e,f], Sami Franssila[c], Piers Andrew[d], Olli Ikkala[a], and Robin H. A. Ras[a,1]

[a]Molecular Materials, Department of Applied Physics, Aalto University (former Helsinki University of Technology), P.O. Box 15100, FI-00076 Aalto, Espoo, Finland; [b]Division of Pharmaceutical Chemistry, Faculty of Pharmacy, University of Helsinki, P.O. Box 56, FI-00014 Helsinki, Finland; [c]Department of Materials Science and Engineering, Aalto University (former Helsinki University of Technology), P.O. Box 13500, FI-00076 Aalto, Espoo, Finland; [d]Nokia Research Center, Broers Building, 21 JJ Thomson Avenue, Madingley Road, Cambridge CB3 0FA, United Kingdom; [e]Department of Physics, Cavendish Laboratory, University of Cambridge, J.J. Thomson Avenue, Cambridge CB3 0HE, United Kingdom; and [f]Department of Physiology, Development, and Neuroscience, University of Cambridge, Downing Street, Anatomy Building, Cambridge CB2 3DY, United Kingdom

Nature offers exciting examples for functional wetting properties based on superhydrophobicity, such as the self-cleaning surfaces on plant leaves and trapped air on immersed insect surfaces allowing underwater breathing. They inspire biomimetic approaches in science and technology. Superhydrophobicity relies on the Cassie wetting state where air is trapped within the surface topography. Pressure can trigger an irreversible transition from the Cassie state to the Wenzel state with no trapped air—this transition is usually detrimental for nonwetting functionality and is to be avoided. Here we present a new type of reversible, localized and instantaneous transition between two Cassie wetting states, enabled by two-level (dual-scale) topography of a superhydrophobic surface, that allows writing, erasing, rewriting and storing of optically displayed information in plastrons related to different length scales.

micropillars | silicone nanofilaments | optical data storage | bistable | two-tier

The lotus plant has become famous by its ability to always keep its leaves clean and dry (1), making superhydrophobic wettability a vibrant topic of research in recent years (2). However, nature also offers other concepts for exploiting nonwettability, in particular layers of trapped air (*plastrons*) that some underwater insects maintain within the hair growing on their exterior to keep them dry or to serve as a physical gill (3, 4). Plastrons on immersed artificial superhydrophobic surfaces have been under active study as well (5–9). Because the formation of an air layer between water and the surface is the essential feature of superhydrophobic surfaces in general, a transition from a state with an air layer (Cassie state) to a state where it is lost (Wenzel state) means loss of nonwetting properties (10, 11). Therefore, superhydrophobic surfaces are typically designed to provide the most stable Cassie state possible using hydrophobic surface chemistry and rough microtopography (12).

Reversing the Cassie-Wenzel transition is very challenging (13–16)—in particular for immersed surfaces (involving a plastron, see Fig. 1) where it has so far only been accomplished by electrochemical generation of gas on the surface to create a new plastron (17) or by exploiting the expansion of gas at low pressure (18). Hierarchical topographies are known to improve the stability of the Cassie state (19) (as well as to promote mechanical resilience, ref. 20, and nonwettability, ref. 21), but it is less widely realized that complex topographies also provide new approaches to wetting state switching by giving rise to a larger number of wetting states, making the term "Cassie state" less well defined: there exist several possible states that involve trapped air, but vary in terms of wetted solid fraction and the volume of the air layer (4, 22, 23). Wetting hysteresis depends on the amount of wetted solid, so states with little wetting are of particular interest for designing bistable systems.

Here we present, for the first time, reversible and localized pressure-induced transitions between two distinct Cassie-type wetting states on a hierarchical superhydrophobic surface immersed in water. The states arise from the two topographical levels on the surface: a pattern of silicon microposts and a superhydrophobic nanofilament coating grown on the microtopography (Fig. 1B). In one wetting state the plastron occupies the space between the microposts—we call this state the *micro-Cassie* state as the plastron has micron-scale dimensions. In the other state the space between the posts is mostly filled with water but air still remains in the nanofilament layer, which is only hundreds of nanometers thick. Because of this thin plastron, the state is also of the Cassie type because the water-solid contact area fraction is small. This state is called the *nano-Cassie* state, accordingly. We will show that the wetting states can be locally and reversibly switched by using a nozzle to cause pressure-driven transitions (Fig. 1B).

Results

Superhydrophobic surfaces with two-level topography were constructed from silicon wafers patterned with a square array (pitch 20 μm) of cylindrical microposts (diameter 10 μm, height 5 or 10 μm) that are further coated with silicone nanofilaments (24–26). The nanofilaments are themselves superhydrophobic (advancing and receding contact angles of planar coating $170°/145° \pm 5°$), which is necessary for a stable nano-Cassie state.

Submerging the hierarchical surface in water leads to the formation of a plastron in the micro-Cassie state. A local switching to the nano-Cassie state can be induced by "writing" with a jet of water (see Fig. 1B). The dynamic pressure of the jet gives rise to Laplace pressure (pressure difference between water and plastron) that pushes the water between the microposts, causing a localized and immediate transition. Calculations predict a transition Laplace pressure of 6.9 kPa (see *SI Text*). Yet, even a large pressure will not cause a transition to the Wenzel state due to the high stability of the plastron within the nanofilaments. An optical micrograph of a nano-Cassie/micro-Cassie boundary is shown in Fig. 2A.

Unlike the Wenzel to Cassie transition, the nano-Cassie to micro-Cassie transition involves only a low kinetic barrier due to the small amount of wetted solid in the nano-Cassie state. In fact, the micro-Cassie state is energetically more stable than the nano-Cassie state (see *SI Text*). We were able to restore the

Fig. 1. Wetting states and transitions between them on surfaces with different topographies. (*A*) With single-level topography, positive Laplace pressure causes a transition from the Cassie to the Wenzel state. The transition involves wetting of the whole solid surface and is irreversible in most cases. (*B*) Hierarchical topography. Nanofilaments suppress the transition to the Wenzel state and positive Laplace pressure will cause a transition to the nano-Cassie state instead, where wetted solid area remains small due to the plastron in the nanofilament layer. This transition can be reversed by negative Laplace pressure. Constant pressure in the plastron is maintained by a gas reservoir such as a macroscopic bubble on the edge of the surface. Scale bar in the scanning electron micrographs is 10 µm (in the inset, 500 nm). The post height in the micrographs is 5 µm.

micro-Cassie state by a reverse writing process: local negative Laplace pressure was built between water and the plastron by sucking water with the needle close to the surface, causing the plastron to fill the space between the posts once again (see Fig. 1*B*). According to our calculations (*SI Text*) the nano-Cassie state becomes unstable at a Laplace pressure between −5.0 kPa and −1.3 kPa. The local transitions do not alter the pressure of the plastron because a gas reservoir (like an air bubble on the surface shown in Fig. 3*A*) will store and release air as needed.

For comparison with the hierarchical topography, we also fabricated a superhydrophobic surface with single-level topography (see Fig. 1*A*) by coating a micropatterned silicon surface with a hydrophobic fluoroalkylsilane monolayer (advancing and receding contact angles of coating on flat surface 118°/102° ± 3°) instead of nanofilaments. The plastron on an immersed single-level surface is in the Cassie state, and the water jet writing technique shown in Fig. 1*A* can be used to cause a local Cassie-Wenzel transition, which is irreversible.

To study in detail the shape of the water-air interface in the micro-Cassie and nano-Cassie states we introduced a new laser scanning confocal imaging technique that makes use of fluorescent polymer nanoparticles dispersed in the water. Two confocal scanning modes are combined: reflection of 633-nm-wavelength laser light and fluorescence from the nanoparticles that are excited with a 543-nm-wavelength laser light. The reflection signal provides information on topography while the fluorescent nanoparticles help to differentiate water from air. Fig. 2*B* shows a series of micrographs of the boundary between nano-Cassie and micro-Cassie regions, focused 15, 10, 5 and 0 µm above the sub-

strate. The fluorescence image shows that, while the space between the posts in the micro-Cassie region is filled with air, in the nano-Cassie region water occupies most of the space except the filament layer, as depicted in the schematic picture in Fig. 2*B*.

The interference fringes in the reflectance images—caused by interference between reflections from the water-air interface and the air-silicon interface at the bottom—reveal the shape of the water-air interface. The vertical distance between two intensity maxima corresponds to a half of the wavelength of the laser light, 317 nm. The interface starts to curve downwards about 30 µm from the boundary between the micro-Cassie and nano-Cassie states with the slope increasing close to the boundary.

Although water fills most of the space between the posts in the nano-Cassie state, the "coronae" surrounding the posts in the microscope images in Fig. 2 suggest that micrometer-sized pockets of air still remain around the bases of the posts (see also Figs. S1 and S2). Indeed, theoretical considerations (see *SI Text*) show that small air pockets are expected to remain in the corners between the posts and the bottom if the advancing contact angle of the nanopattern is greater than 135°. Negative Laplace pressure is shown (*SI Text*) to destabilize the air pockets, ultimately inducing transition to micro-Cassie state.

Fig. 3*A* shows a sample with two-level topography and another with single-level topography in water. The sample with two-level topography is mostly in the micro-Cassie state but has regions, made in the shape of letters ("2 TIER"), which are in the nano-Cassie state. These regions appear remarkably bright due to intense light scattering. In fact, nano-Cassie regions exhibit an order of magnitude stronger scattering intensity than micro-

Fig. 2. The boundary between nano-Cassie and micro-Cassie states. (*A*) Optical microscope images of a nano-Cassie/micro-Cassie boundary, one focused at the post tops and the other at the bottom. In the nano-Cassie region the posts are surrounded by "coronae" that are pockets of remaining air. (*B*) Combined confocal images where the reflectance scan is shown in greyscale while fluorescence signal coming from dispersed nanoparticles is shown in green (false color). When the confocal plane is below 10 μm, nanoparticles are seen only in the nano-Cassie region where water fills most of the space between posts. A schematic interpretation is below the images. The diameter and height of silicon posts is 10 μm.

Cassie regions, leading to substantial optical contrast (see Fig. S3). The scattering is caused by the curved interface between water and the air pockets around the bases of the posts that cause reflections to a wide range of angles (see Fig. S2). Unlike nano-Cassie regions, Wenzel regions on single-level topography (letters "1 TIER" in Fig. 3*A*) do not scatter much due to the absence of a water-air interface.

The difference in terms of wettability between the nano-Cassie and the Wenzel state is demonstrated in Fig. 3*B*, which shows the samples from Fig. 3*A* after water has been drained out. A thin film of water stays on the Wenzel regions on the single-level surfaces and assembles into droplets, while the two-level surface emerges completely dry: this is because the nano-Cassie state is nonwetting whereas Wenzel is wetting.

Fig. 3*C* confirms that although the nanofilament layer is just hundreds of nanometers thick and thus the nano-Cassie plastron is very thin, air can still flow through it to form a micro-Cassie region inside a larger nano-Cassie region.

Fig. 3. Writing and erasing patterns. (*A*) A jet of water has been used to create letter-shaped regions of Wenzel and nano-Cassie state in the plastrons of single-level (1-tier) and two-level (2-tier) topography surfaces, respectively. The escaping air pushed aside by the jet has formed into macroscopic bubbles that act as gas reservoirs (indicated by arrows in the figure). (*B*) Water has been drained from the container. The sample with single-level topography has small droplets where the letters have been, whereas the sample with hierarchical topography has emerged from the water completely dry. (*C*) Demonstrating the reverse transition: a small region of micro-Cassie state is created by suction inside a larger region of nano-Cassie state (created by a jet of water). The inset is a photograph taken with a camera. Scale bar is 40 μm. (*D*) The middle one of the 5 nano-Cassie dots is repeatedly erased (returned to micro-Cassie state) and rewritten. Scale bar is 4 mm.

Discussion

We wish to emphasize that the two wetting states can be thought of as bistable logic states to store binary data. For example, the surface could be divided into an array of dots that represent bits. Also, the optical contrast between the states suggests that such an array of bits could be used for a bistable reflective display. To demonstrate repeated write/erase cycles, we present in Fig. 3*D* a series of photographs of a group of five nano-Cassie dots. The dot in the center is repeatedly erased and rewritten. Furthermore, to verify stability and reversibility even after prolonged storage, a pattern was written on a surface and inspected after 30 days. The pattern was found to be unchanged and still erasable.

Apart from data storage or display applications, we also envision uses in microfluidics. While the micro-Cassie state is expected to have a large slip length (5), the nano-Cassie state most likely involves little slip regardless of the plastron, as water between the microposts is unlikely to flow well. The

micro-Cassie/nano-Cassie transition could enable dynamical creation of configurable flow barriers or fast-flowing channels.

To summarize, we demonstrated reversible bistable switching between two Cassie-type wetting states on a hierarchical superhydrophobic surface and used a novel confocal microscopy technique based on dye-labeled nanoparticles for imaging the plastron. A localized writing/erasing procedure was used for instant switching of wetting state, enabling storage of binary data, and a substantial scattering intensity contrast between the states allows optical reading of information. We believe the result opens a new perspective to wetting-functionalized surfaces as reversibly configurable information-carrying media.

Materials and Methods

Silicon Micropatterning. Microposts were fabricated on (100) silicon wafers. A UV-lithography step defined the patterns of the microposts to a 500 nm thick layer of AZ1505 photoresist (Clariant). Subsequently, cryogenic deep reactive ion etching (Oxford Instruments, Plasmalab 100) was used to etch the microposts in silicon. (temperature $-120\,°C$, inductively coupled plasma power 1,000 W, capacitively coupled plasma power 3 W, pressure 10 mTorr, SF_6 flow 40 sccm, O_2 flow 6 sccm). The etch rate was measured to be 2.0–$2.5\,\mu m/$ min. After etching, the remaining photoresist was removed in acetone.

Deposition of Nanofilament and Fluoroalkylsilane Coatings. For nanofilament deposition, patterned silicon samples were kept in oxygen plasma (Gatan Solarus Model 950) for 5 minutes to increase the density of surface OH groups (plasma power 65 W, pressure 70 mTorr, O_2 flow 40 sccm). Samples were then placed to a glass reaction vessel (volume ca. 1 L) which was flushed with humidified argon (relative humidity 30%). After flushing, the gas inlet and outlet were closed and ca. 100 μl of methyltrichlorosilane (Sigma-Aldrich, 99%) was injected with a syringe through a silicone septum into a Teflon cup inside the vessel. After at least 14 hours the samples were taken out and rinsed with deionized water. Fluoroalkylsilane coatings were made in a similar manner except the vessel was flushed with dry argon and $CF_3(CF_2)_5(CH_2)_2SiCl_3$ precursor (ABCR, 97%) was used (injected amount was ca. 30 μl).

Scanning Electron Microscopy. Scanning electron microscopy was performed on a JEOL JSM-7500FA field-emission microscope. Micrographs were taken at 5 kV voltage.

Optical Microscopy. A Leica DM4500 P optical microscope was used with an immersion objective. Photographs were taken with a Leica DFC 420 camera.

Confocal Imaging. Samples were immersed in water containing fluorescently labelled nanoparticles (Fluoro-Max red fluorescent polymer microspheres, 0.21 μm diameter, Thermo Scientific). Confocal laser scanning microscopy (LSM 510, Zeiss, Germany; 25 × water immersion objective, NA = 0.8) was used to record z-stacks of the samples. Interfaces between media with different refractive indices (e.g., water and air) were visualized by recording the reflection of a HeNe laser ($\lambda = 633$ nm), fluorescence of the beads was measured with a second HeNe laser ($\lambda = 543$ nm). For visualization, the fluorescence signal was superimposed on the reflectivity signal (Fig. 2B). Noise was removed from the fluorescence signal by Gaussian convolution and removal of low-intensity pixels. Unmodified data is shown in Fig. S4.

Wetting Transitions. Switching between micro-Cassie and nano-Cassie states was done using a syringe or a pressurized hose and a needle with a nonbeveled tip. The pressurized hose could be used to provide a steady pressure for careful drawing (Fig. 3A) whereas a syringe could be used for both blowing (micro-Cassie to nano-Cassie transition) and sucking (nano-Cassie to micro-Cassie transition) water. Surfaces with 5 μm tall posts were used for reversible writing and erasing.

Light Scattering Intensity Measurement. Sample (in a petri dish filled with water) was illuminated from above with light focused on either a nano-Cassie or micro-Cassie region. Scattered light was collected with an optical fiber directed at the illuminated spot at an angle of 55° relative to the surface normal. The intensity as a function of wavelength was measured with an Ocean Optics USB4000-VIS-NIR spectrometer.

1. Barthlott W, Neinhuis C (1997) Purity of the sacred lotus, or escape from contamination in biological surfaces. *Planta* 202:1–8.
2. Liu K, Yao X, Jiang L (2010) Recent developments in bio-inspired special wettability. *Chem Soc Rev* 39:3240–3255.
3. Flynn MR, Bush JWM (2008) Underwater breathing: The mechanics of plastron respiration. *J Fluid Mech* 608:275–296.
4. Balmert A, Bohn HF, Ditsche-Kuru P, Barthlott W (2011) Dry under water: Comparative morphology and functional aspects of air-retaining insect surfaces. *J Morphol* 272:442–451.
5. McHale G, Newton MI, Shirtcliffe NJ (2010) Immersed superhydrophobic surfaces: Gas exchange, slip and drag reduction properties. *Soft Matter* 6:714–719.
6. Poetes R, Holtzmann K, Franze K, Steiner U (2010) Metastable underwater superhydrophobicity. *Phys Rev Lett* 105:166104.
7. Rathgen H, Sugiyama K, Ohl CD, Lohse D, Mugele F (2007) Nanometer-resolved collective micromeniscus oscillations through optical diffraction. *Phys Rev Lett* 99:214501.
8. Lei L, Li H, Shi J, Chen Y (2010) Diffraction patterns of a water-submerged superhydrophobic grating under pressure. *Langmuir* 26:3666–3669.
9. Bobji MS, Kumar SV, Asthana A, Govardhan RN (2009) Underwater sustainability of the "Cassie" state of wetting. *Langmuir* 25:12120–12126.
10. Lafuma A, Quéré D (2003) Superhydrophobic states. *Nat Mater* 2:457–460.
11. Dorrer C, Rühe J (2009) Some thoughts on superhydrophobic wetting. *Soft Matter* 5:51–61.
12. Marmur A (2003) Wetting on hydrophobic rough surfaces: To be heterogeneous or not to be? *Langmuir* 19:8343–8348.
13. Krupenkin TN, Taylor JA, Wang EN, Kolodner P, Hodes M, Salamon TR (2007) Reversible wetting-dewetting transitions on electrically tunable superhydrophobic nanostructured surfaces. *Langmuir* 23:9128–9133.
14. Boreyko JB, Chen CH (2009) Restoring superhydrophobicity of Lotus leaves with vibration-induced dewetting. *Phys Rev Lett* 103:174502.
15. Manukyan G, Oh JM, Van Den Ende D, Lammertink RGH, Mugele F (2011) Electrical switching of wetting states on superhydrophobic surfaces: A route toward reversible Cassie-to-Wenzel transitions. *Phys Rev Lett* 106:014501.
16. Kumari N, Garimella SV (2011) Electrowetting-induced dewetting transitions on superhydrophobic surfaces. *Langmuir* 27:10342–10346.
17. Lee C, Kim CJ (2011) Underwater restoration and retention of gases on superhydrophobic surfaces for drag reduction. *Phys Rev Lett* 106:14502.
18. Forsberg P, Nikolajeff F, Karlsson M (2011) Cassie-Wenzel and Wenzel-Cassie transitions on immersed superhydrophobic surfaces under hydrostatic pressure. *Soft Matter* 7:104–109.
19. Nosonovsky M (2007) Multiscale roughness and stability of superhydrophobic biomimetic interfaces. *Langmuir* 23:3157–3161.
20. Verho T, et al. (2011) Mechanically durable superhydrophobic surfaces. *Adv Mater* 23:673–638.
21. Koch K, Bhushan B, Jung YC, Barthlott W (2009) Fabrication of artificial Lotus leaves and significance of hierarchical structure for superhydrophobicity and low adhesion. *Soft Matter* 5:1386–1393.
22. Sajadinia SH, Sharif F (2010) Thermodynamic analysis of the wetting behavior of dual scale patterned hydrophobic surfaces. *J Colloid Interface Sci* 344:575–583.
23. Boreyko JB, Baker CH, Poley CR, Chen CH (2011) Wetting and dewetting transitions on hierarchical superhydrophobic surfaces. *Langmuir* 27:7502–7509.
24. Gao L, McCarthy TJ (2006) A perfectly hydrophobic surface ($\theta_A/\theta_R = 180°/180°$). *J Am Chem Soc* 128:9052–9053.
25. Artus GRJ, et al. (2006) Silicone nanofilaments and their application as superhydrophobic coatings. *Adv Mater* 18:2758–2762.
26. Rollings DE, Veinot JGC (2008) Polysiloxane nanofibers via surface initiated polymerization of vapor phase reagents: A mechanism of formation and variable wettability of fiber-bearing substrates. *Langmuir* 24:13653–13662.

APPLIED PHYSICAL SCIENCES

Supporting Information

Verho et al. 10.1073/pnas.1204328109

SI Text

Energetics of the Micro-Cassie to Nano-Cassie Transition. Calculating the free energy difference of the micro-Cassie and nano-Cassie states is no different from calculating the Cassie-Wenzel transition energy for a single level topography, except that the equilibrium (Cassie-Baxter) contact angle of the nanofilaments has to be taken as the Young's contact angle of the microposts. The free energy change during the transition is

$$\Delta G = (\gamma_{sl} - \gamma_s)\Delta A_{sl} + \gamma \Delta A_l, \qquad [\text{S1}]$$

where ΔA_{sl} is the increase of solid-liquid contact area and ΔA_l is the change of liquid-air interfacial area. γ, γ_s and γ_{sl} are the liquid-air, solid-air and liquid-solid interfacial tensions, respectively. Using A_b as the area of the bottom in a unit cell and $2\pi r_p h$ as the area of the post sidewalls, we arrive at, using the Young's equation $\cos\theta_Y = (\gamma_s - \gamma_{sl})/\gamma$,

$$\Delta G = \gamma(-\cos\theta_Y(A_b + 2\pi r_p h) - A_b). \qquad [\text{S2}]$$

The micro-Cassie state is energetically favorable if $\Delta G > 0$. This is the case if

$$\cos\theta_Y < -\frac{A_b}{A_b + 2\pi r_p h}. \qquad [\text{S3}]$$

For the micropattern discussed in this study, with a post height of 5 μm, the inequality is satisfied with θ_Y larger than 132°. The equilibrium contact angle of the nanofilament coating is clearly larger than this, which implies that the micro-Cassie is the lower energy state.

Micro-Cassie to Nano-Cassie Transition. By a force balance consideration, we can calculate the critical Laplace pressure Δp_c for the micro-Cassie to nano-Cassie transition. The transition occurs when the meniscus depins from the edges of the posts and moves toward the bottom (see Fig. S1A). We proceed under the assumption that the shape of the meniscus around each post is approximately identical across the area under the water jet, which is reasonable because the diameter of the water jet is much larger than the size scale of the micropattern. The downward force per unit cell exerted on the meniscus by the Laplace pressure is

$$F_{lp} = A_b \Delta p, \qquad [\text{S4}]$$

where Δp is the Laplace pressure. The balancing upward force caused by surface tension at the edges of the posts has the value

$$F_\gamma = -2\pi r_p \gamma \cos\theta, \qquad [\text{S5}]$$

where θ is the contact angle that the meniscus makes with the sidewall of the post. In equilibrium $F_\gamma = F_{lp}$. The forces are largest when θ equals the advancing contact angle of the sidewalls θ_A (the advancing contact angle of the nanofilament coating). The Laplace pressure is then

$$\Delta p_c = -\frac{2\pi r_p}{A_b}\gamma\cos\theta_A. \qquad [\text{S6}]$$

The advancing contact angle of the nanofilament coating is roughly 170°, which gives $\Delta p_c = 6.9$ kPa. For comparison, for

single level topography with a fluorinated coating with an advancing angle of 120° one gets $\Delta p_c = 3.5$ kPa.

Axisymmetric Meniscus Shape. Consider the microscopic meniscus on the sidewall of a micropost shown in Fig. S1B. Assuming cylindrical symmetry, we write the vertical force balance for the part of the meniscus indicated in the figure. The surface tension on the contact line acts to pull the meniscus upwards, while the Laplace pressure Δp and the surface tension at r tend to push the meniscus toward the bottom. The force balance reads

$$\pi(r^2 - r_p^2)\Delta p + 2\pi r_p\gamma\cos\theta + 2\pi r\gamma\sin\alpha = 0, \qquad [\text{S7}]$$

where r_p is the post radius and γ is the surface tension. The sine of α can be expressed in terms of the derivative dz/dr as

$$\sin\alpha = \left(1 + \frac{1}{(dz/dr)^2}\right)^{-\frac{1}{2}}. \qquad [\text{S8}]$$

Inserting [S8] into [S7] yields

$$\frac{dz}{dr} = -\left[\left(\frac{r}{r_p\cos\theta + \frac{\Delta p}{2\gamma}(r^2 - r_p^2)}\right)^2 - 1\right]^{-1}. \qquad [\text{S9}]$$

This result will be used below. In addition, we remark that this equation can also be used to calculate approximate shapes of the meniscus close to the micro-Cassie to nano-Cassie transition, although in reality the shape will not be perfectly axisymmetric.

Air Pockets at the Bases of the Posts. During a Cassie-Wenzel transition, the water immediately wets the bottom of the micropattern once it makes contact with it. However, in the case of two level topography (micro-Cassie/nano-Cassie transition) the bottom and the sidewalls are coated with superhydrophobic nanofilaments which have a very high advancing contact angle. In this case, there remain ring-shaped air pockets around the bases of the posts (a micrograph is shown in Fig. S2).

Fig. S1C depicts the situation. After the transition to nano-Cassie state, while the pressure is still on, the contact angle at the post sidewall and at the bottom equals θ_A. Applying Eq. S7 with $\alpha = \theta_A$ and $\theta = \theta_A$ we get

$$r = \frac{\gamma}{\Delta p}\left[-\sin\theta_A + \sqrt{\sin^2\theta_A - \frac{r_p\Delta p}{\gamma}\left(2\cos\theta_A - \frac{r_p\Delta p}{\gamma}\right)}\right], \qquad [\text{S10}]$$

which gives the width of the air pocket as $r - r_p$. For $\Delta p = 7$ kPa, i.e., just enough to cause a transition to nano-Cassie state, the width of the air pockets would be 4.6 μm (with $r_p = 5$ μm and $\theta_A = 170°$). We can thus see that a larger pressure is needed to wet most of the bottom (Fig. S1D shows the shape of the air pocket with $\Delta p = 10$ kPa). The pocket width always has a finite value with any Δp, so at least in theory there always remains an air pocket. On the other hand, we can see from Eq. S7 that with $\Delta p \geq 0$ one must have $\cos\theta < -\sin\theta$ (i.e., $\theta_A < 135°$) for an air pocket to exist. Therefore air pockets will not be found on single level topographies.

When Laplace pressure is removed, the air pocket assumes a zero curvature shape (see Fig. S1D for an example). The receding contact angle θ_R of the nanocoating dictates the minimum width

the pocket must have in the final state. Using [S7] with $\Delta p = 0$, we find

$$r_{\min} = -\frac{\cos \theta_R}{\sin \theta_R} r_p. \qquad \textbf{[S11]}$$

If $r_{\min}$ is large enough, the air pockets of adjacent posts coalesce and the nano-Cassie state becomes unstable. This will happen if

$$\cos \theta_R \leq -\left(\frac{r_p^2}{(L/2)^2} + 1\right)^{-\frac{1}{2}}, \qquad \textbf{[S12]}$$

where L is the pitch of the micropattern. For the geometry used in this study we find that the air pockets coalesce for receding angles more than 153.4°. In other words, too hydrophobic a nanopattern leads to an unstable nano-Cassie state.

Negative Laplace Pressure and Reverse Transition. When a negative Laplace pressure is produced by suction, the air pockets at the bases of the posts begin to expand, governed by the magnitude of Δp and θ_R. An example shape is shown in Fig. S1D. The width of the air pocket is determined by equation similar to [S10]:

$$r = \frac{\gamma}{\Delta p}\left[-\sin \theta_R \pm \sqrt{\sin^2 \theta_R - \frac{r_p \Delta p}{\gamma}\left(2\cos \theta_R - \frac{r_p \Delta p}{\gamma}\right)}\,\right]. \qquad \textbf{[S13]}$$

Of the two solutions the one corresponding to a minus sign can be deemed unphysical because with $\Delta p \to 0^-$ we would have $r \to \infty$. The physical solution (corresponding to plus sign) is consistent with [S11] with $\Delta p = 0$ and increases with decreasing pressure. However, a negative enough pressure renders the determinant (expression under square root) negative, restricting the maximum size of the air pocket.

With a negative Δp, the air pocket can be destabilized by two ways. First, the determinant in Eq. S13 may become negative implying that no stable solution exist. This occurs with pressures lower than

$$\Delta p_{c,1} = \frac{\gamma}{r_p}\left(\cos \theta_R - \sqrt{2\cos^2 \theta_R - 1}\right). \qquad \textbf{[S14]}$$

However, if the air pockets grow large enough to coalesce before $\Delta p_{c,1}$ is reached, they become unstable at a pressure less negative than $\Delta p_{c,1}$. Depending on θ_R, this will happen if the radius corresponding to $\Delta p_{c,1}$ is larger than $L/2$. The receding angle value θ_R^* for which $r = L/2$ at $\Delta p_{c,1}$ is given by the equation

$$\sin \theta_R^* = \frac{L/2}{r_p}\left(\cos \theta_R^* - \sqrt{2\cos \theta_R^* - 1}\right). \qquad \textbf{[S15]}$$

With $\theta_R > \theta_R^*$, the air pockets will coalesce at the Laplace pressure

$$\Delta p_{c,2} = -\frac{2\gamma}{r_p}\frac{\frac{L/2}{r_p}\sin \theta_R + \cos \theta_R}{\left(\frac{L/2}{r_p}\right)^2 - 1}. \qquad \textbf{[S16]}$$

The actual critical pressure for the nano-Cassie to micro-Cassie transition can thus be written as

$$\Delta p_c = \begin{cases} \Delta p_{c,1} & \text{if } \theta_R < \theta_R^* \\ \Delta p_{c,2} & \text{if } \theta_R > \theta_R^* \end{cases} \qquad \textbf{[S17]}$$

Δp_c depends strongly on θ_R and obviously goes to zero when equality in [S12] applies. In this study, Δp_c ranges between -5.0 kPa and -1.3 kPa (corresponding to $\theta_R = 145 \pm 5°$).
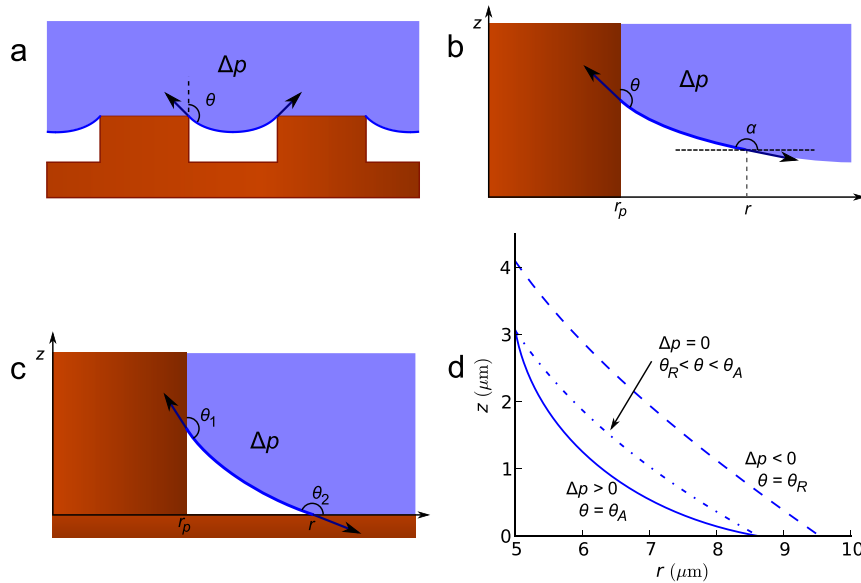

Fig. S1. Microscopic meniscus shape. (A) Deformation of the meniscus under Laplace pressure. The surface tension counters the force caused by pressure. (B) Schematic representation of Eq. **S7** in *SI Text*. (C) An air pocket at the base of a post. (D) Air pocket shapes calculated by integrating Eq. **S9**. From *Left* to *Right*: $\Delta p = 10$ kPa, the state after the water has been pushed between the posts by pressure ($\theta_A = 170°$); $\Delta p = 0$, the pressure has been released; $\Delta p = -3$ kPa, negative pressure is generated by suction ($\theta_R = 145°$).
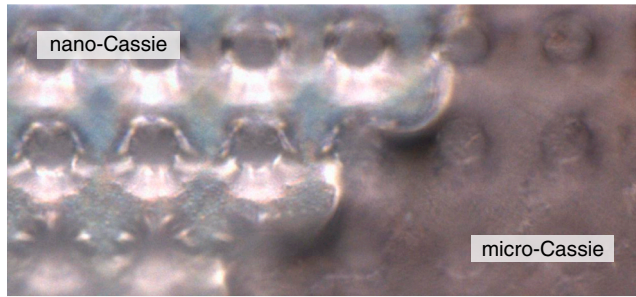
Fig. S2. An optical micrograph of a micro-Cassie/nano-Cassie boundary. The sample is tilted by 22° so that horizontal water-air interfaces do not reflect incident light to the objective. Consequently interfaces with a nonhorizontal slope appear brightest. Due to this, the air pockets at the bases of the posts are shown clearly. It is also obvious that the nano-Cassie region is much brighter overall due reflections from the interfaces between the air pockets and water. Because of the tilt and the shallow depth of field of the objective, only one row of posts is in focus in the image.
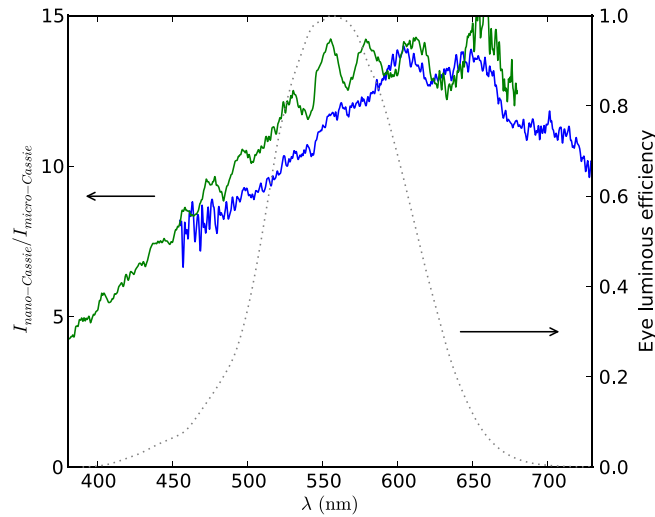
Fig. S3. Light scattering contrast. Solid lines: the light scattering intensity ratio $I_{nano\text{-}Cassie}/I_{micro\text{-}Cassie}$ as a function of wavelength (blue curve measured with a tungsten light source, green curve measured with a mercury-vapor light source). Dotted line: eye sensitivity (photopic function, source: http://www.cvrl.org/lumindex.htm). In the range where eye is sensitive the nano-Cassie state scatters 8–14 times more than the micro-Cassie state.
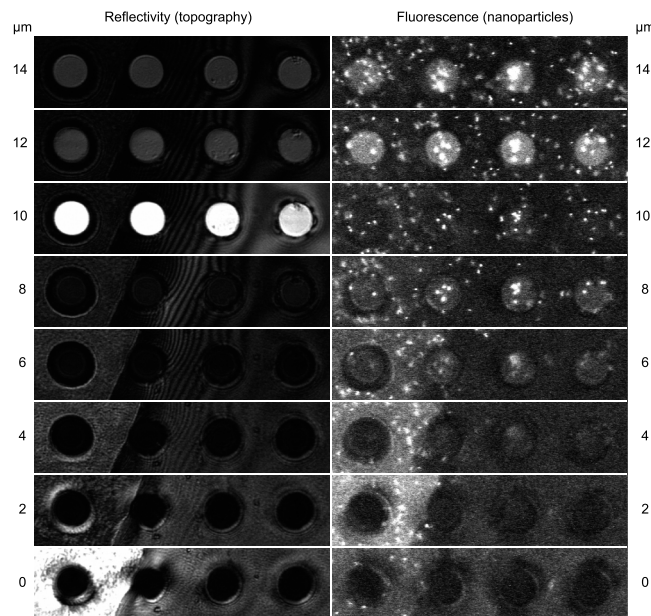

Fig. S4. Original confocal microscopy data without noise removal or contrast adjustment. Images were taken every 1 μm, but only every other image is shown here to conserve space. Conventional reflectivity scan is shown on the *Left*, while fluorescence signal from nanoparticles is shown in the *Right*.